Narrowband Organic Light-Emitting Diodes for Fluorescence Microscopy and Calcium Imaging

*Caroline Murawski, Andreas Mischok, Jonathan Booth, J. Dinesh Kumar, Emily Archer, Laura Tropf, Chang-Min Keum, Ya-Li Deng, Kou Yoshida, Ifor D. W. Samuel, Marcel Schubert, Stefan R. Pulver, and Malte C. Gather**

Dr. Caroline Murawski,[+] Dr. Andreas Mischok, Jonathan Booth, Dr. J. Dinesh Kumar, Emily Archer, Dr. Laura Tropf, Dr. Chang-Min Keum, Ya-Li Deng, Dr. Kou Yoshida, Prof. Ifor D. W. Samuel, Dr. Marcel Schubert, Prof. Malte C. Gather

Organic Semiconductor Centre, SUPA

School of Physics and Astronomy

University of St Andrews

St Andrews KY16 9SS, UK

E-mail: mcg6@st-andrews.ac.uk

[+] present address: Kurt-Schwabe-Institut für Mess- und Sensortechnik e.V. Meinsberg, Kurt-Schwabe-Str. 4, 04736 Waldheim, Germany

Jonathan Booth, Dr. Stefan R. Pulver

School of Psychology and Neuroscience

University of St Andrews

St Andrews KY16 9JP, UK

* Corresponding author: mcg6@st-andrews.ac.uk

Keyword: OLED, fluorescence microscopy, calcium imaging

Abstract

Fluorescence imaging is an indispensable tool in biology, with applications ranging from single-cell to whole-animal studies and with live mapping of neuronal activity currently receiving particular attention. To enable fluorescence imaging at cellular scale in freely moving animals, miniaturized microscopes and lensless imagers have been developed that can be implanted in a minimally invasive fashion; but the rigidity, size, and potential toxicity of the involved light sources remains a challenge. Here, narrowband organic light-emitting diodes (OLEDs) are developed and used for fluorescence imaging of live cells and for mapping of neuronal activity in *Drosophila melanogaster* via genetically encoded Ca^{2+} indicators. In order to avoid spectral overlap with fluorescence from the sample, distributed Bragg reflectors are integrated onto the OLEDs to block their long-wavelength emission tail, which enables an image contrast comparable to conventional, much bulkier mercury light sources. As OLEDs can be fabricated on mechanically flexible substrates and structured into arrays of cell-sized pixels, this work opens a new pathway for the development of implantable light sources that enable functional imaging and sensing in freely moving animals.

Optical sensing and manipulation of neural activity in the brain holds great promise for neuroscience and medicine due to its potential for minimally invasive interfacing of millions of neurons in parallel.[1,2] The combination of miniaturized implantable light sources with genetically encoded light-activated ion channels already allows targeted activation and inhibition of neural activity.[3–5] However, sensing of neural response, e.g. through genetically encoded calcium indicators (GECI),[6,7] often relies on fibers or light-emitting diodes (LEDs), which are typically limited to low-resolution recording from larger neural populations.[8–10] Alternative approaches use head-mounted microscopes, which enable monitoring the action potentials of individual neurons.[11] Despite great technological advances in this area,[12,13] the imaging optics of these devices makes them bulky, thus potentially influencing animal behavior and likely preventing clinical use. New lensless imaging techniques are now emerging that may eventually shrink the entire microscope to a size that allows implantation.[14,15] However, the development of suitable light sources for fluorescence excitation has received less attention; currently, excitation light is usually provided by lasers or high-power LEDs, with the latter being spectrally filtered to avoid overlap with fluorophore emission.

In this context, organic light-emitting diodes (OLEDs) appear particularly attractive, since they are extremely thin, can be fabricated on flexible and stretchable substrates,[16–18] and may be structured to high-density arrays with cell-scale dimensions.[19–21] In combination with organic photodetectors,[22–25] OLEDs could be integrated on a flexible, pixelated chip that enables both fluorophore excitation and recording of neural activity from a single device. OLEDs consist of a stack of ultra-thin layers of organic materials that are of low toxicity compared to many of the III-V semiconductors used in conventional LEDs. OLEDs provide homogeneous emission from both microscopic and macroscopic areas, offer microsecond or better response times, and allow precise intensity control. While the main application of

OLEDs at present is in displays of mobile phones and TVs, OLEDs have already been used successfully in portable and wearable sensors[26–33] and, more recently, in optogenetics to stimulate neurons[34,35] and control cell behavior[19,20]. However, compared to conventional LEDs based on inorganic III-V semiconductor materials, they provide lower brightness and more broadband emission which may be problematic for fluorescence imaging.

Here, we developed high-power narrowband blue-emitting OLEDs for fluorescence imaging. In order to avoid spectral overlap between the long-wavelength tail of the OLED emission and the emission of the fluorophore to be imaged, we narrowed the OLED spectrum using a high-rejection distributed Bragg reflector (DBR). This design allows us to observe fluorescence from fixed and stained cells as well as from live cells expressing a fluorescent protein, with similar image quality to a fluorescence microscope using a conventional mercury excitation source. We also applied our OLEDs to excite a GECI in the ventral nerve cord (VNC) of a *Drosophila melanogaster* larva and, thus, demonstrated that OLEDs can be used to measure intracellular calcium dynamics.

We selected an OLED structure based on the fluorescent blue emitter molecule, 2,5,8,11-tetra-tert-butylperylene (TBPe), and on doped charge transport layers (**Figure 1**a). Compared to phosphorescent or thermally activated delayed fluorescence emitters which achieve higher intrinsic efficiency due to their ability to harvest triplet states, conventional fluorescent emitters generally show much reduced efficiency roll-off at high brightness (i.e., the drop in efficiency with increasing current density due to bi-molecular annihilation is less prominent)[36], offer significantly higher stability, and require lower drive voltages. Using doped charge transport layers limits the voltage drop upon charge injection and due to Ohmic losses and, thus, reduces drive voltages further. As a result, our devices showed a steep increase in current density with voltage and provided high optical power densities at low voltages (Figure 1b). Ultimately, this will simplify the integration with backplane electronics,

which in the case of complementary metal-oxide-semiconductor (CMOS) designs can be limited to a maximum of 5 V, and will minimize heating of the device and of any adjacent biological material.

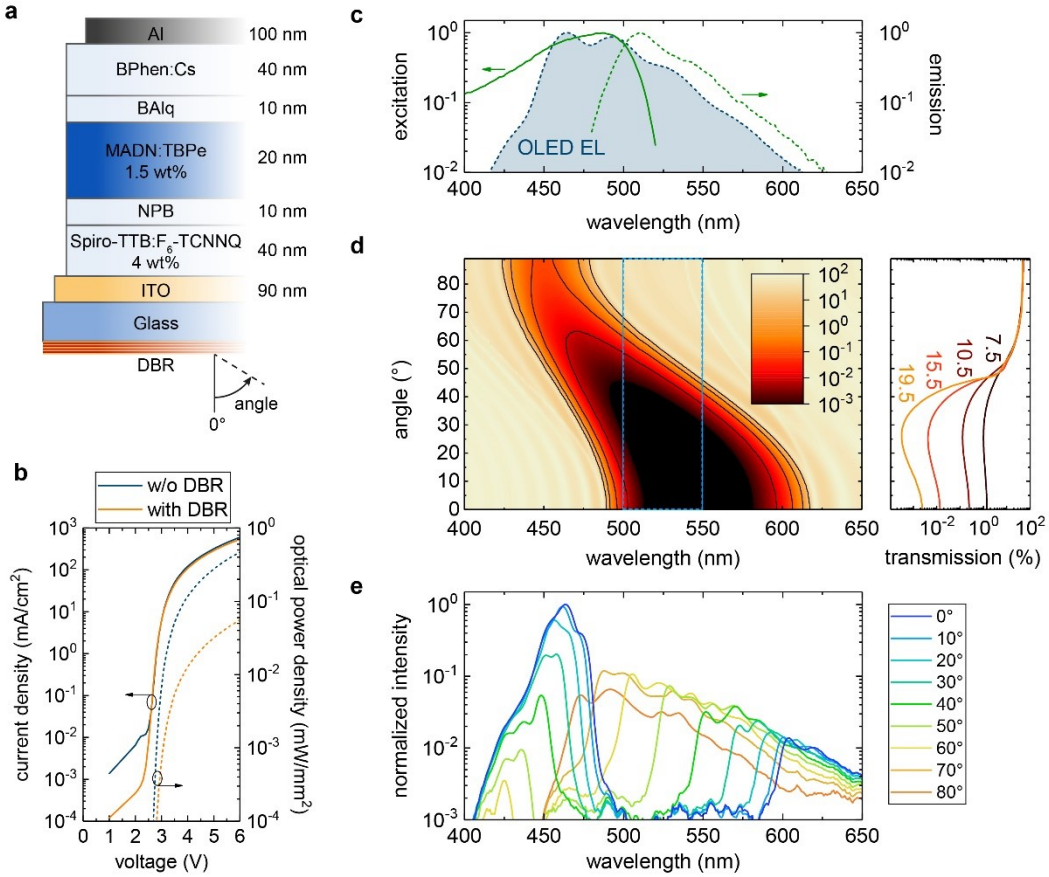

Figure 1. OLEDs with integrated DBRs for fluorescence imaging. a) Device stack used in this study, with indication of the thickness of each layer and definition of the viewing angle. b) Current density (solid lines) and optical power density (dashed lines) as a function of voltage for devices with and without DBR. c) eGFP excitation (solid green line) and emission (dashed green line) and electroluminescence (EL) spectrum of an OLED without DBR emitted in forward direction (blue shaded area). d) Transfer-matrix simulation of DBR transmission spectrum over viewing angle for the DBR used in this study (consisting of 19.5 pairs Ta_2O_5 and SiO_2). Right: Mean transmission between 500 and 550 nm as a function of viewing angle for different DBR structures with 7.5 to 19.5 pairs of Ta_2O_5 and SiO_2. e) EL spectrum of OLED with DBR as a function of viewing angle.

We optimized the OLEDs used in this study for excitation of green emitting proteins and dyes, with a particular focus on enhanced green fluorescent protein (eGFP), which strongly absorbs in the light-blue/sky-blue wavelength regime (peak excitation at 487 nm) and has its emission peak at 510 nm (Figure 1c). The electroluminescence spectra of our bare

OLEDs (i.e., without additional DBR) showed maxima at 464 nm and 492 nm, and had a substantial long-wavelength tail which is a typical characteristic of organic emitters. The emission maxima overlapped well with the eGFP absorption spectrum; however, the tail showed considerable overlap with the eGFP emission. The use of more deep blue emitters could reduce the overlap with eGFP emission, however, will also the decrease the overlap with eGFP absorption thus providing no benefit in overall signal-to-background ratio. Besides, deep blue emitters typically suffer from lower stability and efficiency, which both would be detrimental for successful operation of our devices.

Typical fluorescent protein concentrations in cells range from micro- to millimols per liter.[37,38] For the lower end of this concentration range, only around 0.01 % of the incoming light is absorbed and re-emitted as fluorescence (Methods, Supporting Figure S1). Hence, in order to achieve fluorescence images with high contrast, the OLED emission in the spectral range absorbed by eGFP (i.e., at around 487 nm) needs to be approximately 10,000 times higher than any residual OLED emission within the emission band of eGFP (i.e., at around 510 nm). Due to the small Stokes shift of eGFP, this spectral de-coupling is particularly challenging.[27]

Several strategies have been suggested to make inorganic LEDs[39] and OLEDs[30–32,40,41] compatible with the requirements for fluorescence imaging, including the use of microcavities, DBRs, polarizers, and layers of absorbing molecules. We decided to use DBRs for our work because they offer steep spectral cut-off, high rejection in their stop band and high transmission in their pass band. The transmission characteristics of DBRs fundamentally depend on the angle of incidence. Figure 1d shows a transfer-matrix simulation of the angle-resolved transmission spectrum of a DBR consisting of 19.5 pairs of 64.4 nm Ta_2O_5 and 93.1 nm SiO_2. The layer thickness was optimized for a collection window for fluorescence ranging from 500 to 550 nm. Here, the mean transmission of the DBR remained below 0.01%

for angles of incidence up to 43°. A lower number of DBR pairs reduced the rejection rates in the stop band in forward direction causing more OLED light to overlap with fluorophore emission (Figure 1d and Supporting Figure S2). For higher angles, the transmission in all DBR structures strongly increased due to the blue-shift of the stop band, thus putting an upper limit on the useable numerical aperture of our system.

We fabricated this DBR structure via sputter deposition on a glass substrate and attached it onto the bottom-emitting OLED with a UV curable epoxy. The electrical characteristics of the OLED were unaffected by application of the DBR, however, the optical power density emitted was reduced as the DBR blocks some of the OLED emission (Figure 1b). As intended, in the band between 495 nm and 592 nm the OLED emission in forward direction was suppressed to below the detection limit of our spectrometer (Figure 1e). The blue-shift of the DBR stop band with increasing angle, however, was clearly visible in emission spectra detected off-axis and caused the emission within the long-wavelength sideband to shift into our collection window for GFP fluorescence for detection angles above around 40°. In practice, this means that the fluorescence collection angle should remain limited to < 40°, e.g., by using objectives or lensless imaging systems with a numerical aperture lower than NA = sin(40°) = 0.64. The spectral shift with emission angle furthermore leads to an overall beam-shaping of the OLED light into forward direction, which reduces off-axis excitation of the fluorophore (Supporting Figure S3).

In fluorescence microscopy, image contrast is determined by the ratio of fluorescence from the dye or protein to the overall background signal. The intensity of fluorescence depends on dye/protein concentration, extinction coefficient and PLQY, and on the brightness and spectrum of the excitation source. The background signal will – at least for our case – likely be dominated by light leaking through the DBR, particularly for high detection angles.

To determine the contrast that can be achieved with our device, we used the experimental setup sketched in **Figure 2**a,b. A glass slide with a 70 µm thick cavity containing a solution of pyrromethene 556 (PM556; chemical structure in Figure 2c)[42] was mounted on top of the OLED and the fluorescence intensity was recorded through an upright epi-fluorescence microscope equipped with an emission filter for eGFP (pass band, 500 to 550 nm, Supporting Figure S4) and a cooled sCMOS camera. PM556 is a synthetic dye with similar photoluminescence quantum yield, extinction coefficient, and emission spectrum as eGFP (Supporting Figure S4). Figure 2c shows a calculation of how much of the incident OLED light is absorbed and re-emitted by PM556 as a function of dye concentration. The fluorescence intensity is exponentially increasing up to concentrations of around 2 mmol l^{-1}, where saturation sets in. From this, we selected a concentration range between 0.5 µmol l^{-1} and 2 mmol l^{-1} for our experiments, staying within the range of typical fluorophore concentrations[37,38] and spanning over three orders of magnitude in expected fluorescence intensity.

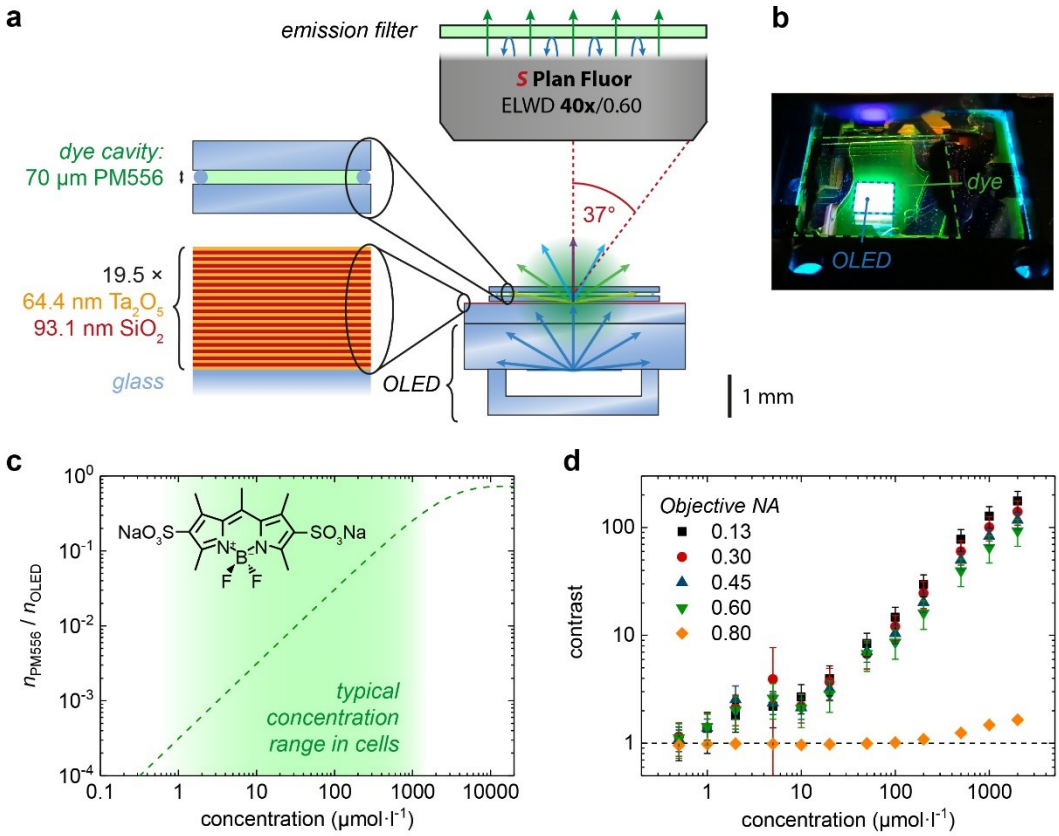

Figure 2. Test of fluorescence contrast achievable with OLED illumination. a) Sketch of the experimental setup. The OLED-DBR-device excites the dye PM556, which is injected into a small glass cavity. Dye emission is imaged through different objectives and an emission filter. The device dimensions along the optical axis are drawn to scale. b) Photograph of the illuminated sample. c) Calculation of the ratio between number of photons emitted by PM556 over number of photons emitted by OLED for varying PM556 concentration. Inset: chemical structure of PM556. d) Measured fluorescence contrast as a function of PM556 concentration for a series of objectives with different numerical aperture (NA). The OLED was driven at 118 mA cm^{-2} and the camera exposure time was 2 s. Error bars represent the standard deviation across the imaged area.

The achievable contrast was then measured for five different objectives with magnifications ranging from 4× to 40× and numerical apertures from 0.13 to 0.80, corresponding to opening angles from 7.5° to 53.1° (Figure 2d, Supporting Table S1). In agreement with the calculation, the fluorescence intensity and contrast strongly increased with increasing concentration and reached values above 90:1 at 2 mmol l^{-1} for all objectives tested, except for the objective with NA = 0.8, where contrast was only 1.6:1 (Figure 2d, Supporting Figure S5). The poor value for the latter objective was due to insufficient suppression of

OLED emission within the detection band at large angles as also confirmed by the much higher background intensity observed for this objective (Supporting Table S1). For the other four objectives, which all have collection angles < 40°, the measured contrast decreased slightly with increasing NA of the objective, which results from their different collection volumes (Supporting Note S1). In conclusion, objectives with NA up to around 0.60 yield good contrast from dye concentrations of around 10 µmol l^{-1} and higher, which is well-compatible with the fluorophore concentrations achievable in cells and tissue.[37,38]

Next, we tested the suitability of OLED illumination to excite fluorescence in fixed tissue slices, live cells and preparations of *Drosophila melanogaster* larvae. For these measurements, we mounted the DBR directly underneath the sample to be imaged and placed the OLED 5.5 mm further below. This arrangement ensured that scattering of excitation light in the samples did not lead to bleed-through of high-angle green emission from the OLED into the fluorescence image (Supporting Figure S6). **Figure 3**a shows fluorescence images of a section of a mouse kidney, in which glomeruli and convoluted tubules were labelled with Alexa Fluor 488 (excitation and emission spectrum of Alexa Fluor 488, Supporting Figure S4), comparing OLED illumination from below the sample to epi-illumination by a conventional Hg lamp. We obtained highly detailed images with excellent contrast under both OLED and Hg lamp illumination with a signal-to-noise ratio (SNR) of 84 ± 9 for the OLED and 480 ± 16 for the Hg-lamp (Supporting Figure S7a). An intensity profile along the dashed line in Figure 3a revealed similarly steep edges and same details for illumination by both the OLED and the Hg lamp (Figure 3e). Furthermore, the fluorescence intensities in different regions of the image showed a high degree of correlation when comparing OLED and Hg lamp illumination (r^2 = 0.91, Supporting Figure S7a and S7c).

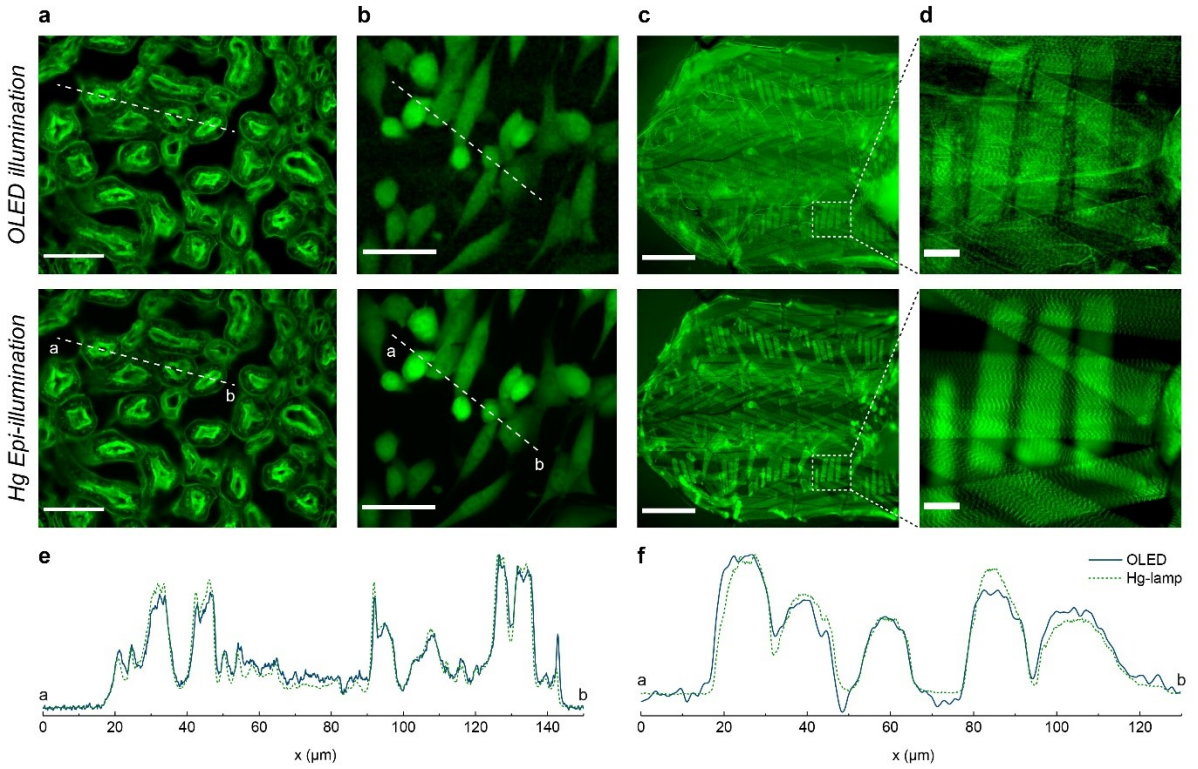

Figure 3. Comparison of fluorescence imaging with OLED trans-illumination and Hg lamp in epi-illumination. a) Stained mouse kidney section with glomeruli and convoluted tubules labelled with Alexa Fluor 488. b) Live culture of NIH/3T3 fibroblasts with cytoplasmic expression of eGFP. c) Semi-intact preparation of a third instar *Drosophila melanogaster* larva with muscle-fusion GFP imaged at 4× magnification. d) Same preparation at 20× magnification. e) Normalized intensity profiles along the dashed lines in the kidney section images shown in a) for OLED illumination (solid line) and for Hg lamp illumination (dashed line). f) Same as before for the dashed lines in the NIH/3T3 fibroblasts images in b). OLED driven at 592 mA cm^{-2} for all images. Scale bars: 50 µm (a, b, d) and 500 µm (c).

Next, we imaged live NIH/3T3 fibroblasts with cytoplasmic expression of eGFP (Figure 3b). The fluorescence images of both OLED and Hg lamp were again similar, however, due to low expression levels of eGFP, the image with OLED illumination was missing some sub-cellular details. This was due to the higher relative noise level under OLED illumination compared to the Hg lamp (Figure 3f). Nevertheless, the absolute fluorescence intensities between OLED and Hg illumination were still highly correlated (r^2 = 0.78, Supporting Figure S7b and S7d)

We also imaged a semi-intact preparation of a laid-out *Drosophila melanogaster* larva expressing muscle-fusion eGFP to explore how the trans-illumination of the OLED compares

to epi-illumination of the Hg-lamp for samples of substantial thickness (Figure 3c and 3d).[43,44] The striated somatic musculature of the larva was well visible with both light sources and individual z-discs could be clearly distinguished. For trans-illumination by the OLED, further structures were visible, which was partly due to light scattering, e.g. at air-filled trachea, and partly because for this case the excitation intensity was highest at the side of the sample that faces away from the light collecting objective. This also caused slight blurring of the image due to out-of-focus fluorescence from lower-lying structures, an effect that is more prominent at lower magnification due to the greater depths of focus, as seen from the lower contrast in Figure 3c compared to Figure 3d.

After demonstrating static fluorescence imaging under OLED excitation, we applied our light source to live imaging of neural activity using a genetically encoded Ca^{2+} indicator (GECI). To observe relevant changes in neural activity, frame rates of at least 2 Hz were required. As a test bed, we imaged the isolated central nervous system (CNS) of a third instar *Drosophila melanogaster* larva with pan-neuronal expression of GCaMP6s[45] – a highly sensitive GECI based on circularly permuted eGFP.[7] Fluorescence was predominantly observed along the segmentally arranged ventral nerve cord (VNC), both in abdominal and thoracic regions (**Figure 4**a). The baseline corrected time-lapse of GCaMP6s fluorescence clearly revealed a dynamic change in activity from anterior to more posterior regions (Figure 4b, Supporting Video S1), indicating fictive backward locomotor activity in the CNS preparation.[45,46] Looking at the temporal evolution of the GCaMP6s intensity along the abdominal region of the VNC (Figure 4c, circular ROIs in Figure 4a), we detected two backward waves within the time of the measurement, with an average wave duration of approximately 6.5 s, similar to previous studies.[45,46] The calcium signal in the thoracic region, however, showed bilaterally asymmetric activity between left and right side

(Figure 4d). This activity pattern is indicative of fictive head sweep behavior, here combined with a backwards wave.[46]

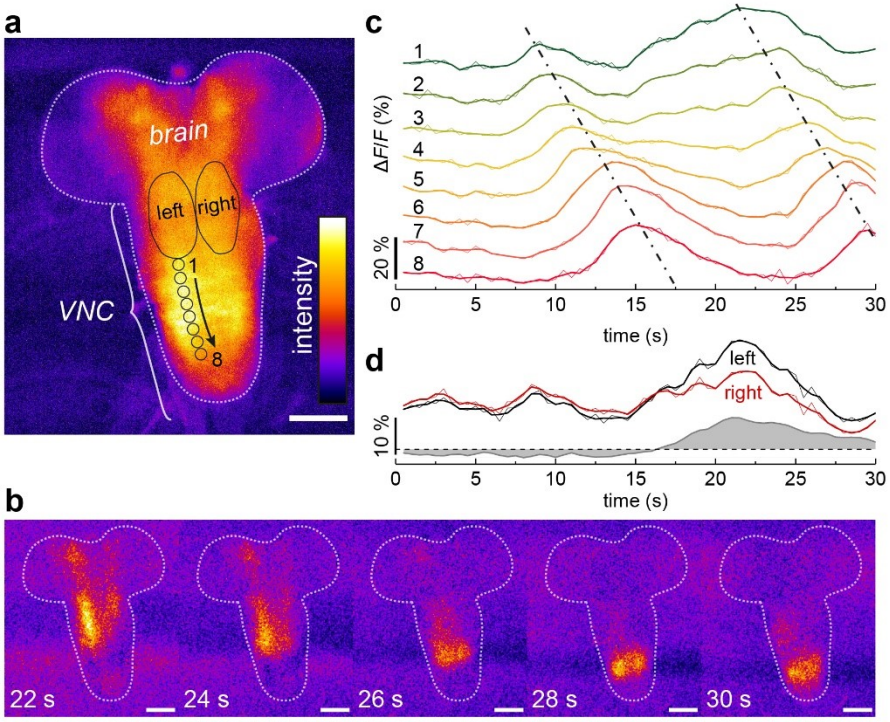

Figure 4. Using OLED illumination for live Ca-imaging of neuronal activity in an isolated CNS preparation of a third instar *Drosophila melanogaster* larva with pan-neuronal expression of GCaMP6s. a) Median fluorescence intensity from a 60 frame time series (false color). b) Individual frames of the time series after subtraction of the non-varying baseline fluorescence (median intensity). c) Mean fluorescence intensity change $\Delta F/F$ over time from the 8 circular ROIs indicated in a). Thin lines: raw data; thick lines: smoothed. Dash-dotted lines indicate waveform activity responsible for fictive backward locomotion (guide to the eye). d) Mean fluorescence intensity change $\Delta F/F$ of left and right sided ROIs at the thorax indicated in a) over time. The difference between both intensities shows bilaterally asymmetric activity indicative of a head sweep (grey shaded area). Results representative of 4 trials. Frame rate, 2 fps. Scale bars: 100 µm.

In conclusion, by narrowing their emission spectrum, we demonstrated that OLEDs can be used for fluorescence imaging. We integrated a high-brightness blue OLED based on doped charge transport layers with a DBR to suppress emission within the spectral emission range of eGFP. These devices allowed us to excite dyes and fluorescent proteins in stained and live cells, and to record fluorescence images that are similar to those obtained with a conventional mercury lamp under epi-illumination.

The angular dependent spectral response of the used DBRs means that the NA of the overall system is limited, with the present DBR design to a maximum value of 0.6. The NA could be increased by stacking DBRs with different stop bands or by gradually adjusting the thickness of the layers forming the DBR. Other, possibly complimentary avenues to narrowing the OLED emission spectrum include the use of more narrow-band emitters such as platinum complexes with a rigid core[47,48] or colloidal quantum dots,[49,50] and applying absorber layers for further spectral filtering.[24,51] Alternatively, shaping the OLED emission profile to have a larger degree of forward direction, e.g., by using photonic structures,[52] micro-lens arrays,[53] or even active steering of the beam direction depending on the objective used,[54] may alleviate the need for filters with a high degree of angular stability.

The potential of OLEDs to be mechanically flexible and to be structured into high-density arrays of cell-sized pixels makes them extremely attractive as implantable light sources. Translation to flexible substrates should be feasible using high-performance thin-film encapsulation[55,56] and recent advances in making flexible DBRs.[57] In addition, the above-mentioned complimentary strategies to narrow down the OLED spectrum are all compliant with flexible substrates. Furthermore, the need for high spectral purity can be relaxed if the OLED is combined with a miniature lensless microscope in a side-by-side configuration, rather than the transmission configuration used here. The flat footprint of such a compact imager would substantially enhance the ability of lensless microscopes to perform functional imaging in awake and behaving mammals, e.g. for real-time monitoring of neuronal activity. A possible further extension is the combination of optical sensing with optical manipulation by integrating spectrally orthogonal OLED light sources, e.g. for independent Ca imaging and optogenetic activation of neurons with cell level resolution. Future development of the OLED excitation source should furthermore focus on achieving higher brightness to reduce the

exposure time for live imaging, and on lateral integration of miniaturized OLEDs with lensless imagers.

Experimental Section

OLED and DBR fabrication: OLEDs were fabricated on glass substrates (1.1 mm thickness) coated with 90 nm thick pre-structured indium tin oxide (ITO), using thermal evaporation at a base pressure of 2×10^{-7} mbar (Angstrom EvoVac). Layer thickness was controlled *in situ* with calibrated quartz crystal monitors. The following materials were used (Figure 1a): 40 nm 2,2',7,7'-tetrakis(N,N'-di-p-methylphenylamino)-9,9'- spirobifluorene (Spiro-TTB) *p*-doped with 2,2'-(perfluoronaphthalene-2,6-diylidene)dimalononitrile (F_6-TCNNQ) (4 wt%) as hole transport layer, 10 nm N,N′-di(naphtalene-1-yl)-N,N'-diphenylbenzidine (NPB) as electron blocking layer, 20 nm 2-methyl-9,10-bis(naphthalen-2-yl)anthracene (MADN) doped with 2,5,8,11-tetra-tert-butylperylene (TBPe) (1.5 wt%) as emission layer, 10 nm bis-(2-methyl-8-chinolinolato)-(4-phenyl-phenolato)-aluminium(III) (BAlq) as hole blocking layer, 40 nm 4,7-diphenyl-1,10-phenanthroline (BPhen) doped with cesium as *n*-doped electron transport layer, and 100 nm aluminum as cathode. Devices were encapsulated under nitrogen atmosphere and directly after fabrication, using a glass lid and a moisture getter using a UV-curable epoxy (Norland NOA68). The device active area was 16.9 mm^2 (4.0 mm × 4.2 mm).

The thicknesses of the different oxide layers forming the DBR were designed by transfer-matrix simulations using complex refractive index data obtained via spectroscopic ellipsometry (M-2000DI, J.A. Woollam Co.). Subsequently, layers were fabricated onto 0.5 mm thick glass substrates via RF sputtering in a vacuum chamber (Angstrom NexDep). Layer thickness was controlled *in situ* with calibrated quartz crystal monitors. The DBR consisted of the following layers: 19 × (64.4 nm Ta_2O_5 / 93.1 nm SiO_2) / 64.4 nm Ta_2O_5.

Device characterization: OLED characteristics were measured with a source-measure unit (Keithley 2400), a calibrated silicon photodiode, and a spectrograph (Oriel MS125) coupled to a CCD camera (Andor DV420-BU). Angle-resolved spectra were measured with an in-house built goniometer setup equipped with a fiber-coupled spectrometer (OceanOptics Maya LSL). The optical power density was calculated taking the angular emission characteristics of the OLED into account.

Characterization of fluorescent solutions: Excitation/emission spectra of disodium-1,3,5,7,8-pentamethylpyrromethene-2,6-disulfonate-difluoroborate (PM556) (0.02 mmol l^{-1} in water) and eGFP (0.3 g l^{-1} in 50:50 water:glycerol) were measured with a fluorometer with detection/excitation wavelength set to 540 nm/483 nm (Edinburgh Instruments FLS980). The spectra shown were smoothed over 5 points using a Savitzky-Golay algorithm.

The ratio of photons emitted by the fluorophore $n_{\text{fluorophore}}$ (PM556 or eGFP) versus photons emitted by the OLED n_{OLED} is calculated as $\frac{n_{\text{fluorophore}}}{n_{\text{OLED}}} = \eta_{\text{PLQY}} \cdot (1 - e^{-cd\varepsilon})$. Here, the photoluminescence quantum yield of PM556 in water is η_{PLQY} = 73 %, the extinction coefficient $\varepsilon_{488\text{ nm}} = 6.1\times10^4$ l mol^{-1} cm^{-1},[42] c denotes the dye concentration, and d the thickness of glass cavity containing the dye solution.

Contrast measurement: All microscopy experiments were performed on an upright epi-fluorescence microscope (Nikon Ni-U), with a Chroma 49002 eGFP filter set, Nikon Intensilight mercury lamp, Andor Neo sCMOS camera, and the following Nikon objectives: 4×/0.13 and 10×/0.30 plan fluor, 20×/0.45 and 40×/0.60 super plan fluor extra-long working distance, and 40×/0.80 fluor water dipping.

For contrast measurements, glass cavities were fabricated by sandwiching a 70 µm glass spacer in between two 150 µm glass substrates and fixing the slides with nail polish at the edges. Starting with the lowest dye concentration, solutions of PM556 in water were

injected from one side into the cavity, allowing capillary forces to drag the solution into the cavity. In order to change the concentration, the next higher concentration was injected from one side, while the lower concentrated solution was removed from the opposite side with a wipe, again using capillary forces. The process was repeated at least four times to ensure a homogeneous distribution of the solution. The glass cavity was mounted on top of the OLED and fluorescence intensity was recorded with 2 s exposure time. The OLED was driven in constant current mode at 118 mA cm^{-2}. For analysis, the mean grey value of a 100 × 100 px^2 area was calculated (ImageJ). The contrast was then calculated as $I_{FL}(c)/I_{water}$, where I_{FL} is the fluorescence intensity as a function of the concentration c and I_{water} is the fluorescence intensity of a slide filled with water, i.e. 0 mmol l^{-1} dye concentration. Errors are calculated from standard deviation across the image area.

Cell culturing and Drosophila melanogaster preparation: The stained section of mouse kidney was obtained commercially (FluoCells prepared slide #3, Invitrogen). NIH/3T3-eGFP fibroblasts were cultured in DMEM medium supplemented with GlutaMAX (Gibco), 10 vol% fetal bovine serum (Thermo Fisher Scientific) and 1 vol% penicillin-streptomycin solution (Gibco). Cells were trypsinised using TrypLE express (Gibco) and seeded in tissue culture treated 35 mm dishes (Thermo Fisher Scientific). Cells were incubated in a humidified incubator at 37 °C and 5 % CO_2 for at least 24 hrs before imaging.

For muscle imaging in larval *Drosophila melanogaster*, feeding 3rd instar larvae with GFP expressed in muscles were used.[44] Individual animals were washed with physiological saline, and then placed in a saline-filled lined dissection dish (made of Sylgard®184, Dowsil).[43] The animals were dissected dorsal-side-up and all internal organs including the brain were removed by cutting away the main trachea and nerve roots before removal with forceps.

Fluorescence imaging: Brightness and contrast of all images was adjusted and background was subtracted using a rolling ball filter with sliding paraboloids (1000 px for Figure 3a, 90 px for Figure 3b, 500 px for Figure 3c (only with the Hg lamp), ImageJ). The stained mouse kidney section and the NIH/3T3-cells were imaged through the 40×/0.60 objective. Images of GFP-expressing *Drosophila melanogaster* larvae were taken with a 4×/0.13 and 20×/0.45 objective. For the 3T3-image with OLED illumination 2×2 binning was used (no binning was applied for the other images) and an FFT bandpass filter between 4 and 500 px was applied to suppress horizontal stripe noise from the CMOS chip.

Mean grey values and standard deviation (SD) (Figure 3e and 3f and Supporting Figure S7) were calculated from raw images. For the NIH/3T3 fibroblasts, the FFT bandpass filter was applied to the OLED image (as above) and a 2×2 binning (average intensity) was applied to the Hg-lamp image in order to use the same ROIs for both OLED and Hg-lamp. No further post-processing was applied. The SNR was calculated from intensity *I* and SD of a bright region and a region showing only background (see red ROIs in Supporting Figure S7) as $\mathrm{SNR} = \frac{I_{\mathrm{bright}} - I_{\mathrm{background}}}{\mathrm{SD}_{\mathrm{background}}}$.

Ca-imaging: For Ca-imaging, a third instar *Drosophila melanogaster* larva stably expressing 20XUAS-IVS-GCaMP6s in 57C10-GAL4 was used.[45] In a similar dissection as above, the CNS was isolated and adhered to a 150 µm thick glass slide coated with poly-D-lysine, which enabled good adherence of the CNS to the slide. This coverslip was then carefully removed from the dissection dish and superfused with fresh saline immediately prior to imaging. The preparation was imaged using a 10×/0.30 objective. An FFT bandpass filter between 0 and 2000 px with line removal was applied to suppress horizontal line noise. For the median intensity image (Figure 4a), background was subtracted (rolling ball, radius 1000 px). For the data with baseline subtraction (Figure 4b), the median intensity was subtracted from each frame of the FFT-filtered video and a Gaussian blur of 2 pixel radius

was applied. Average fluorescence intensity ΔF (Figure 4c and 4d) from different ROIs was calculated from the FFT-filtered, Gaussian blurred, background subtracted images. F was calculated from a z-projection of the minimum intensity of the image stack. Data were smoothed over 5 points using a Savitzky-Golay algorithm. Wave durations were calculated from Figure 4c as the time difference in peak intensity between lines 1 and 7.

Supporting information

Supporting Information is available from the Wiley Online Library or from the author.

Acknowledgements

We are grateful for financial support from the Leverhulme Trust (RPG-2017-231), the EPSRC NSF-CBET lead agency agreement (EP/R010595/1, 1706207), the DARPA NESD program (N66001-17-C-4012) and the RS Macdonald Charitable Trust. C.M. acknowledges funding from the European Commission through a Marie Skłodowska Curie individual fellowship (703387). A.M. acknowledges funding through an individual fellowship of the Deutsche Forschungsgemeinschaft (404587082). Y.D. acknowledges support from the Chinese Scholarship Council (CSC). L.T. acknowledges studentship funding through the EPSRC CM-CDT (EP/L015110/1). M.S. acknowledges funding by the Royal Society (Dorothy Hodgkin Fellowship, DH160102). The datasets supporting this publication can be accessed via the PURE repository at https://doi.org/xxx.

Received: ((will be filled in by the editorial staff))
Revised: ((will be filled in by the editorial staff))
Published online: ((will be filled in by the editorial staff))

References

[1] P. R. Roelfsema, D. Denys, P. C. Klink, *Trends Cogn. Sci.* **2018**, *22*, 598.

[2] T. H. Kim, Y. Zhang, J. Lecoq, J. C. Jung, J. Li, H. Zeng, C. M. Niell, M. J. Schnitzer, *Cell Rep.* **2016**, *17*, 3385.

[3] K. L. Montgomery, A. J. Yeh, J. S. Ho, V. Tsao, S. Mohan Iyer, L. Grosenick, E. A. Ferenczi, Y. Tanabe, K. Deisseroth, S. L. Delp, A. S. Y. Poon, *Nat. Methods* **2015**, *12*, 969.

[4] A. D. Mickle, S. M. Won, K. N. Noh, J. Yoon, K. W. Meacham, Y. Xue, L. A. McIlvried, B. A. Copits, V. K. Samineni, K. E. Crawford, D. H. Kim, P. Srivastava, B. H. Kim, S. Min, Y. Shiuan, Y. Yun, M. A. Payne, J. Zhang, H. Jang, Y. Li, H. H. Lai, Y. Huang, S.-I. Park, R. W. Gereau, J. A. Rogers, *Nature* **2019**, *565*, 361.

[5] M. T. Alt, E. Fiedler, L. Rudmann, J. S. Ordonez, P. Ruther, T. Stieglitz, *Proc. IEEE* **2017**, *105*, 101.

[6] A. Miyawaki, J. Llopis, R. Heim, J. M. McCaffery, J. A. Adams, M. Ikura, R. Y. Tsien, *Nature* **1997**, *388*, 882.

[7] T. W. Chen, T. J. Wardill, Y. Sun, S. R. Pulver, S. L. Renninger, A. Baohan, E. R. Schreiter, R. A. Kerr, M. B. Orger, V. Jayaraman, L. L. Looger, K. Svoboda, D. S. Kim, *Nature* **2013**, *499*, 295.

[8] L. Lu, P. Gutruf, L. Xia, D. L. Bhatti, X. Wang, A. Vazquez-Guardado, X. Ning, X. Shen, T. Sang, R. Ma, G. Pakeltis, G. Sobczak, H. Zhang, D. Seo, M. Xue, L. Yin, D. Chanda, X. Sheng, M. R. Bruchas, J. A. Rogers, *Proc. Natl. Acad. Sci.* **2018**, *115*, E1374.

[9] M. Murayama, E. Pérez-Garci, T. Nevian, T. Bock, W. Senn, M. E. Larkum, *Nature* **2009**, *457*, 1137.

[10] G. Cui, S. B. Jun, X. Jin, M. D. Pham, S. S. Vogel, D. M. Lovinger, R. M. Costa, *Nature* **2013**, *494*, 238.

[11] M. R. Warden, J. A. Cardin, K. Deisseroth, *Annu. Rev. Biomed. Eng.* **2014**, *16*, 103.

[12] K. K. Ghosh, L. D. Burns, E. D. Cocker, A. Nimmerjahn, Y. Ziv, A. El Gamal, M. J. Schnitzer, *Nat. Methods* **2011**, *8*, 871.

[13] D. Aharoni, B. S. Khakh, A. J. Silva, P. Golshani, *Nat. Methods* **2019**, *16*, 11.

[14] J. K. Adams, V. Boominathan, B. W. Avants, D. G. Vercosa, F. Ye, R. G. Baraniuk, J. T. Robinson, A. Veeraraghavan, *Sci. Adv.* **2017**, *3*, 1.

[15] Y. Wu, A. Ozcan, *Methods* **2018**, *136*, 4.

[16] M. S. White, M. Kaltenbrunner, E. D. Głowacki, K. Gutnichenko, G. Kettlgruber, I. Graz, S. Aazou, C. Ulbricht, D. a. M. Egbe, M. C. Miron, Z. Major, M. C. Scharber, T. Sekitani, T. Someya, S. Bauer, N. S. Sariciftci, *Nat. Photonics* **2013**, *7*, 811.

[17] T. Sekitani, H. Nakajima, H. Maeda, T. Fukushima, T. Aida, K. Hata, T. Someya, *Nat. Mater.* **2009**, *8*, 494.

[18] J. Liang, L. Li, X. Niu, Z. Yu, Q. Pei, *Nat. Photonics* **2013**, *7*, 817.

[19] A. Steude, M. Jahnel, M. Thomschke, M. Schober, M. C. Gather, *Adv. Mater.* **2015**, *27*, 7657.

[20] A. Steude, E. C. Witts, G. B. Miles, M. C. Gather, *Sci. Adv.* **2016**, *2*, e1600061.

[21] O. Prache, *Displays* **2001**, *22*, 49.

[22] K.-J. Baeg, M. Binda, D. Natali, M. Caironi, Y.-Y. Noh, *Adv. Mater.* **2013**, *25*, 4267.

[23] T. N. Ng, W. S. Wong, M. L. Chabinyc, S. Sambandan, R. A. Street, *Appl. Phys. Lett.* **2008**, *92*, 213303.

[24] B. Siegmund, A. Mischok, J. Benduhn, O. Zeika, S. Ullbrich, F. Nehm, M. Böhm, D. Spoltore, H. Fröb, C. Körner, K. Leo, K. Vandewal, *Nat. Commun.* **2017**, *8*, 15421.

[25] S. Rezaei-Mazinani, A. I. Ivanov, C. M. Proctor, P. Gkoupidenis, C. Bernard, G. G. Malliaras, E. Ismailova, *Adv. Mater. Technol.* **2018**, *3*, 1700333.

[26] A. K. Bansal, S. Hou, O. Kulyk, E. M. Bowman, I. D. W. Samuel, *Adv. Mater.* **2015**, *27*, 7638.

[27] F. Krujatz, O. R. Hild, K. Fehse, M. Jahnel, A. Werner, T. Bley, *Chem. Sci. J.* **2016**, *7*, DOI 10.4172/2150-3494.1000134.

[28] C. M. Lochner, Y. Khan, A. Pierre, A. C. Arias, *Nat. Commun.* **2014**, *5*, 5745.

[29] H. Lee, E. Kim, Y. Lee, H. Kim, J. Lee, M. Kim, H.-J. Yoo, S. Yoo, *Sci. Adv.* **2018**, *4*, eaas9530.

[30] J. Shinar, R. Shinar, *J. Phys. D. Appl. Phys.* **2008**, *41*, 133001.

[31] Z. Shu, F. Kemper, E. Beckert, R. Eberhardt, A. Tünnermann, *RSC Adv.* **2017**, *7*, 26384.

[32] A. Pais, A. Banerjee, D. Klotzkin, I. Papautsky, *Lab Chip* **2008**, *8*, 794.

[33] F. Lefèvre, A. Chalifour, L. Yu, V. Chodavarapu, P. Juneau, R. Izquierdo, *Lab Chip* **2012**, *12*, 787.

[34] A. Morton, C. Murawski, S. R. Pulver, M. C. Gather, *Sci. Rep.* **2016**, *6*, 31117.

[35] A. Morton, C. Murawski, Y. Deng, C. Keum, G. B. Miles, J. A. Tello, M. C. Gather, *Adv. Biosyst.* **2019**, *3*, 1800290.

[36] C. Murawski, K. Leo, M. C. Gather, *Adv. Mater.* **2013**, *25*, 6801.

[37] Y. Chen, L.-N. Wei, J. D. Muller, *Proc. Natl. Acad. Sci.* **2003**, *100*, 15492.

[38] P. Lu, C. Vogel, R. Wang, X. Yao, E. M. Marcotte, *Nat. Biotechnol.* **2007**, *25*, 117.

[39] Y. Sunaga, M. Haruta, H. Takehara, Y. Ohta, M. Motoyama, T. Noda, K. Sasagawa, T. Tokuda, J. Ohta, in *IEEE Biomed. Circuits Syst. Conf.* (Eds.: H. Hirschberg, S.J. Madsen, E.D. Jansen, Q. Luo, S.K. Mohanty, N. V. Thakor), **2014**, p. 89280L.

[40] M. Jahnel, B. Beyer, M. Thomschke, K. Fehse, F. Krujatz, K. Leo, *Electronics* **2015**, *4*, 982.

[41] M. Scholles, L. Kroker, U. Vogel, J. Krüger, R. Walczak, J. Ruano-Lopez, in *Proc. SPIE* (Eds.: H. Becker, W. Wang), **2010**, p. 75930C.

[42] M. Shah, K. Thangaraj, M.-L. Soong, L. T. Wolford, J. H. Boyer, I. R. Politzer, T. G. Pavlopoulos, *Heteroat. Chem.* **1990**, *1*, 389.

[43] A. Fushiki, M. F. Zwart, H. Kohsaka, R. D. Fetter, A. Cardona, A. Nose, *Elife* **2016**, *5*, 1.

[44] S. Crisp, J. F. Evers, A. Fiala, M. Bate, *Development* **2008**, *135*, 3707.

[45] W. C. Lemon, S. R. Pulver, B. Höckendorf, K. McDole, K. Branson, J. Freeman, P. J. Keller, *Nat. Commun.* **2015**, *6*, 7924.

[46] S. R. Pulver, T. G. Bayley, A. L. Taylor, J. Berni, M. Bate, B. Hedwig, *J. Neurophysiol.* **2015**, *114*, 2564.

[47] G. Li, T. Fleetham, E. Turner, X.-C. Hang, J. Li, *Adv. Opt. Mater.* **2015**, *3*, 390.

[48] T. Fleetham, G. Li, L. Wen, J. Li, *Adv. Mater.* **2014**, *26*, 7116.

[49] X. Dai, Z. Zhang, Y. Jin, Y. Niu, H. Cao, X. Liang, L. Chen, J. Wang, X. Peng, *Nature* **2014**, *515*, 96.

[50] Y. Shirasaki, G. J. Supran, M. G. Bawendi, V. Bulović, *Nat. Photonics* **2013**, *7*, 13.

[51] Y.-K. R. Wu, A. E. Hollowell, C. Zhang, L. J. Guo, *Sci. Rep.* **2013**, *3*, 1194.

[52] S. Zhang, G. a. Turnbull, I. D. W. Samuel, *Adv. Opt. Mater.* **2014**, *2*, 343.

[53] L. Zhou, G.-L. Bai, X. Guo, S. Shen, Q.-D. Ou, Y.-Y. Fan, *Appl. Phys. Lett.* **2018**, *112*, 201902.

[54] F. Fries, M. Fröbel, P. Y. Ang, S. Lenk, S. Reineke, *Light Sci. Appl.* **2018**, *7*, 18.

[55] J. Meyer, P. Görrn, F. Bertram, S. Hamwi, T. Winkler, H. H. Johannes, T. Weimann, P. Hinze, T. Riedl, W. Kowalsky, *Adv. Mater.* **2009**, *21*, 1845.

[56] F. Nehm, H. Klumbies, C. Richter, A. Singh, U. Schroeder, T. Mikolajick, T. Mönch, C. Hoßbach, M. Albert, J. W. Bartha, K. Leo, L. Müller-Meskamp, *ACS Appl. Mater. Interfaces* **2015**, *7*, 22121.

[57] C. Liu, Q. Zhang, D. Wang, G. Zhao, X. Cai, L. Li, H. Ding, K. Zhang, H. Wang, D. Kong, L. Yin, L. Liu, G. Zou, L. Zhao, X. Sheng, *Adv. Opt. Mater.* **2018**, *6*, 1800146.

Table of contents entry:

For the first time, organic light-emitting diodes (OLEDs) are used as light source for fluorescence microscopy. Spectral multiplexing enables high contrast and results in fluorescence images of live cells with similar image quality to conventional illumination. Furthermore, the device is applied to recording neuronal activity of small animal models at video rates.

Keyword: OLED, fluorescence microscopy, calcium imaging

*Caroline Murawski, Andreas Mischok, Jonathan Booth, J. Dinesh Kumar, Emily Archer, Laura Tropf, Chang-Min Keum, Ya-Li Deng, Kou Yoshida, Ifor D. W. Samuel, Marcel Schubert, Stefan R. Pulver, and Malte C. Gather**

Narrowband Organic Light-Emitting Diodes for Fluorescence Microscopy and Calcium Imaging

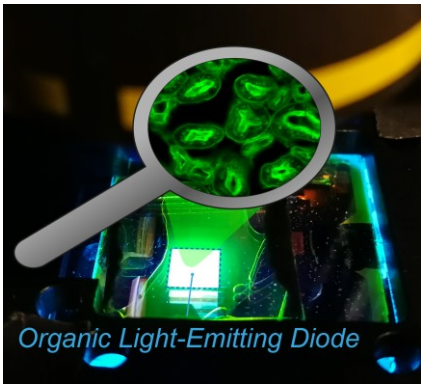

Supporting Information

Narrowband Organic Light-Emitting Diodes for Fluorescence Microscopy and Calcium Imaging

*Caroline Murawski, Andreas Mischok, Jonathan Booth, J. Dinesh Kumar, Emily Archer, Laura Tropf, Chang-Min Keum, Ya-Li Deng, Kou Yoshida, Ifor D. W. Samuel, Marcel Schubert, Stefan R. Pulver, and Malte C. Gather**

Dr. Caroline Murawski,[+] Dr. Andreas Mischok, Jonathan Booth, Dr. J. Dinesh Kumar, Emily Archer, Dr. Laura Tropf, Dr. Chang-Min Keum, Ya-Li Deng, Dr. Kou Yoshida, Prof. Ifor D. W. Samuel, Dr. Marcel Schubert, Prof. Malte C. Gather
Organic Semiconductor Centre, SUPA
School of Physics and Astronomy
University of St Andrews
St Andrews KY16 9SS, UK
E-mail: mcg6@st-andrews.ac.uk

[+] present address: Kurt-Schwabe-Institut für Mess- und Sensortechnik e.V. Meinsberg, Kurt-Schwabe-Str. 4, 04736 Waldheim, Germany

Jonathan Booth, Dr. Stefan R. Pulver
School of Psychology and Neuroscience
University of St Andrews
St Andrews KY16 9JP, UK

* Corresponding author: mcg6@st-andrews.ac.uk

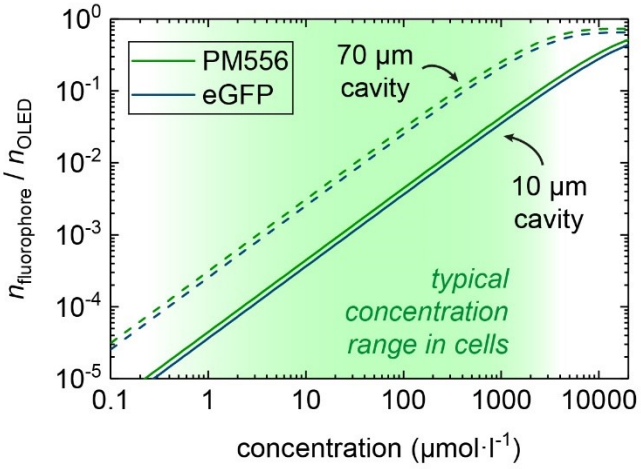

Figure S1. Concentration dependence of fluorophore emission vs. OLED emission. PM556 and eGFP show similar dependence due to their similar absorption and PLQY (PM556:[1] η_{PLQY} = 73 %, $\varepsilon_{488\ nm}$ = 6.1×10^4 l mol^{-1} cm^{-1}; eGFP:[2] η_{PLQY} = 60-70 % (assumed 65% for calculations), $\varepsilon_{488\ nm}$ = 5.6×10^4 l mol^{-1} cm^{-1}). The calculations are displayed for the 70 µm cavity used in experiment and for comparison also for a 10 µm cavity, which resembles roughly the thickness of a cell. At very high concentrations, the ratio saturates due to complete absorption of the excitation light and reaches a value given chiefly by the PLQY of the material.

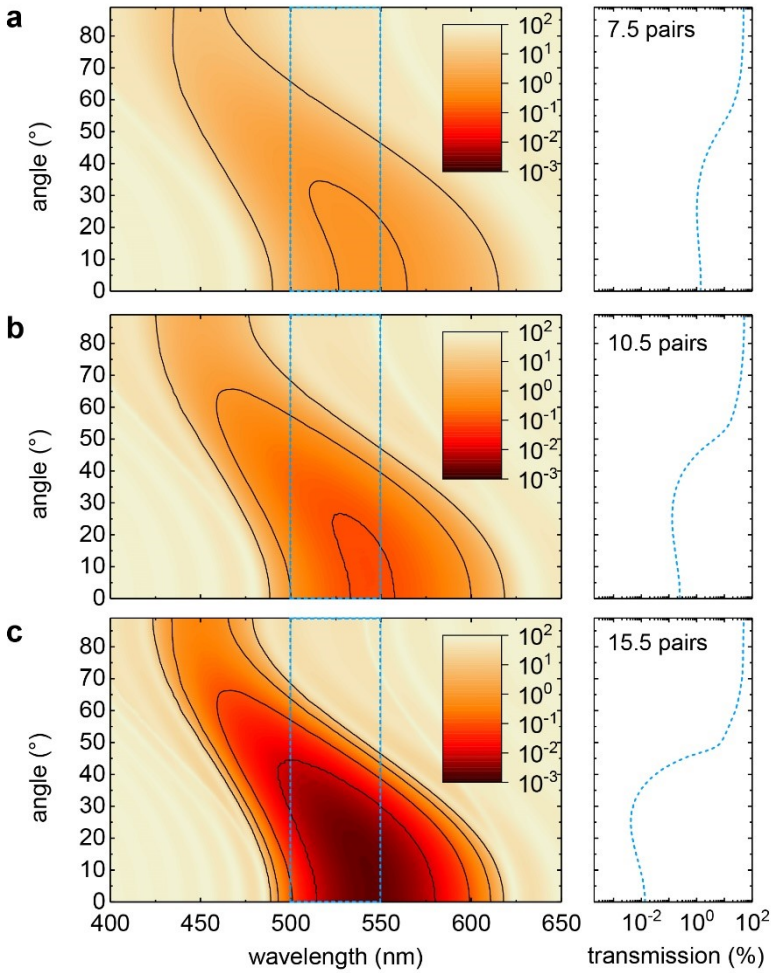

Figure S2. Transfer-matrix simulations of transmission (in %) as function of wavelength and angle for DBR structures with a) 7.5 pairs, b) 10.5 pairs, and c) 15.5 pairs of 64.4 nm Ta_2O_5 and 93.1 nm SiO_2. Right: Mean transmission between 500 nm and 550 nm.

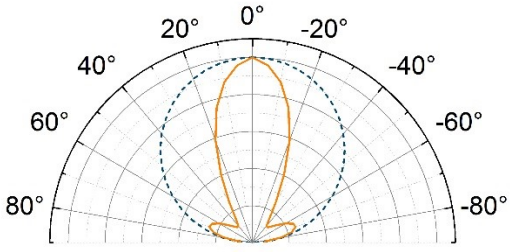

Figure S3. Angular characteristics show strong forward emission for the OLED with DBR (orange solid line) compared to Lambertian assumption (blue dashed line).

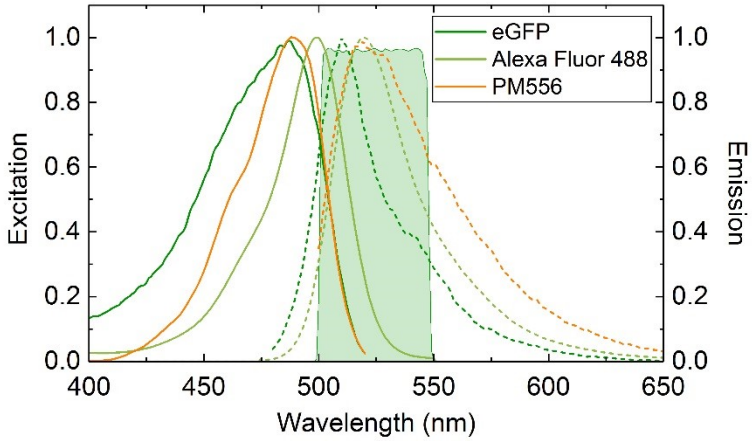

Figure S4. Excitation (solid lines) and emission (dashed lines) spectra of eGFP solution, Alexa Fluor 488 (data from ThermoFisher),[3] and PM556 (0.02 mmol l^{-1} in water). The green shaded area marks the transmission spectrum of the emission filter and dichroic mirror used.

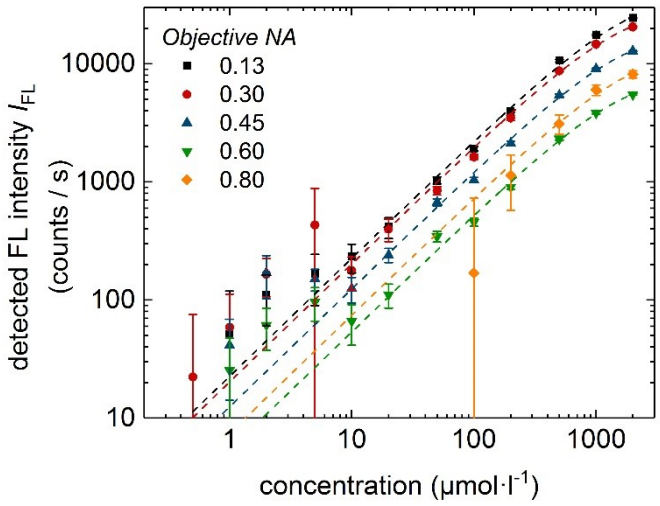

Figure S5. PM556 fluorescence intensity I_{FL} as a function of concentration for different objectives. Errors show standard deviation. Dashed lines show fits according to $I_{\mathrm{FL}} = I_{\mathrm{OLED}} \cdot \eta_{\mathrm{PLQY}} \cdot (1 - e^{-cd\varepsilon})$, which reveal the expected increase of dye fluorescence with concentration for concentrations from 10 µmol l^{-1}.

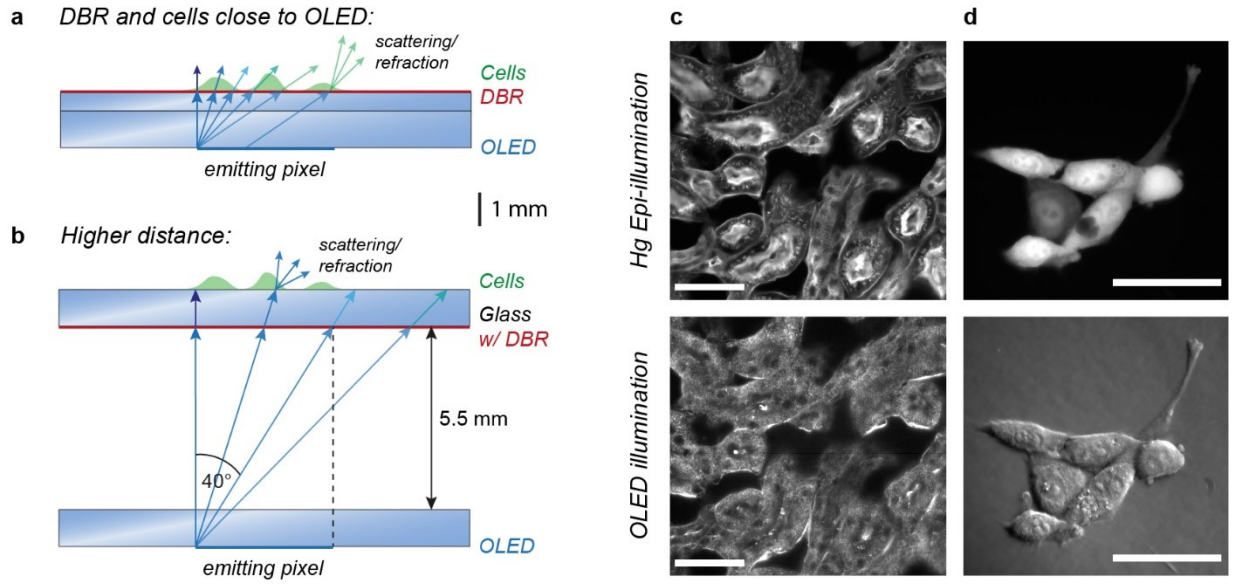

Figure S6. Fluorescence imaging for cells in close distance to the OLED. a,b) Sketch of the experimental setup. a) Configuration used for determining the contrast (see Fig. 2 in the paper). Green light transmitted through the DBR at large angles may be scattered into the forward direction by objects on the sample. b) Configuration used for fluorescence imaging. Due to the larger distance, all light at shallower angles hits the sample outside the field of view. c,d) Fluorescence images obtained with the Hg lamp in epi-illumination (top) and with OLED illumination (bottom) as sketched in a. c) Stained mouse kidney section and d) live NIH/3T3 fibroblasts. For OLED illumination in this configuration, the overlap of the fluorescence signal with scattered light gives an image impression similar to dark field (c) or phase contrast (d) microscopy images. Scale bars: 50 µm.

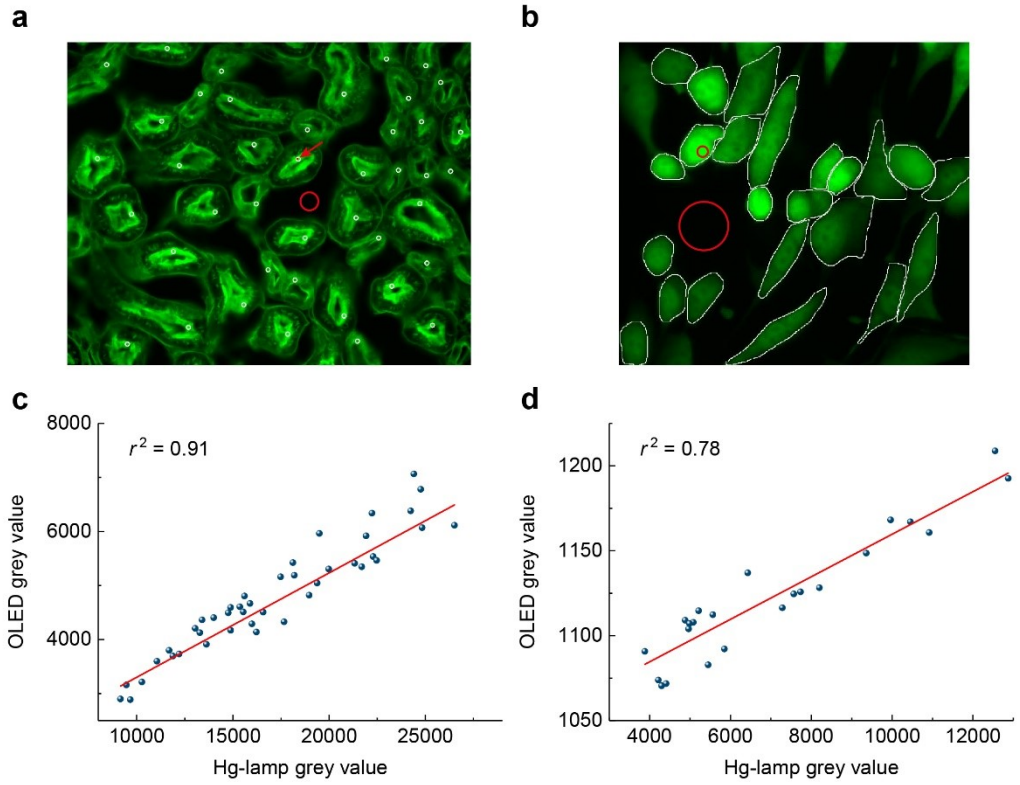

Figure S7. Comparison of cell fluorescence intensities with OLED illumination and mercury lamp in epi-illumination for the stained mouse kidney section (a,c) and for live culture of NIH/3T3 fibroblasts (b,d). a,b) Fluorescence images obtained with the mercury lamp display regions of interest (ROIs) used for comparing cell intensities. Red ROIs are used to calculate SNR (see Methods); white ROIs are used for measuring the mean grey value of cells. For c), circular ROIs of 15 px diameter are used while for d) the mean grey value of whole cells is measured. c,d) Linear regression (red line) of OLED versus mercury lamp grey values (blue dots).

Table S1. List of objectives used and measured fluorescence intensities.

Magnification	NA	Angle (°)	Contrast	I_{FL} (cts/s)	I_{water} (cts/s)	I_{FL}/I_{theo}
4×	0.13	7.5	176.5	24,363	139	1.00
10×	0.30	17.5	140.2	20,488	147	0.98
20×	0.45	26.7	116.7	12,796	111	1.03
40×	0.60	36.9	93.2	5,502	60	1.03
40×	0.80	53.1	1.6	8,153	12,597	0.87

Angle: opening angle to air
Contrast: achieved contrast at 2 mmol l^{-1} PM556
I_{FL}: measured fluorescence intensity
I_{water}: background intensity of a slide filled with water (0 mmol l^{-1})
I_{FL}/ I_{theo}: measured over calculated fluorescence intensity at 2 mmol l^{-1}, normalized to the 4× objective

Note S1. In epi-illumination, excitation light is projected through the objective onto the sample leading to different spot sizes and, thus, increased excitation densities at higher magnification. With the OLED illumination from below, however, the excitation density is independent of the objective. However, the area that is projected through the different objectives onto each pixel of the camera still decreases with increasing magnification. This leads to lower fluorescence intensity per pixel at higher magnifications. This is partly off-set by the increase in numerical aperture with increasing magnification. In order to take these effects into account, we calculated the ratio of measured fluorescence intensity I_{FL} to theoretical intensity I_{theo} at 2 mmol l^{-1} concentration, where $I_{FL} = (I_{2\,mM} - I_{water})$ and $I_{theo} \sim NA^2 \cdot A$, with A as the detected area. The results are given in Supplementary Table S1 and Supplementary Fig. S5. For objectives with NA up to 0.60, only small deviations from unity are observed, while for the objective with NA of 0.80, the measured ratio is smaller than expected due to the large collection of background intensity at higher angles.

Video S1. Ca-imaging of neuronal activity using OLED illumination. Isolated CNS preparation of third instar *Drosophila melanogaster* larva with pan-neuronal expression of GCaMP6s. Left: Fluorescence intensity of GCaMP6s (false colour). Right: Fluorescence intensity with median background subtracted (see methods in main paper). Videos are displayed at 10 times real-time speed. Scale bars: 100 µm

References

[1] M. Shah, K. Thangaraj, M.-L. Soong, L. T. Wolford, J. H. Boyer, I. R. Politzer, T. G. Pavlopoulos, *Heteroat. Chem.* **1990**, *1*, 389.

[2] N. C. Shaner, P. A. Steinbach, R. Y. Tsien, *Nat. Methods* **2005**, *2*, 905.

[3] https://www.thermofisher.com/de/de/home/life-science/cell-analysis/labeling-chemistry/fluorescence-spectraviewer.html; accessed on 28/11/18.